GPS Solutions (2023) 27:130
https://doi.org/10.1007/s10291-023-01468-8

ORIGINAL ARTICLE

Estimation of GLONASS inter-frequency clock bias considering the phase center offset differences on the L3 signal

Jiaqi Wu[1] · Xingxing Li[1] · Yongqiang Yuan[1] · Xin Li[1,2] · Hongjie Zheng[1] · Wei Zhang[1]

Received: 16 March 2023 / Accepted: 29 April 2023 / Published online: 19 May 2023

Abstract

GLONASS has been transmitting the code division multiple access navigation signals on the third band L3 for six GLONASS-M+and three GLONASS-K satellites, in addition to the legacy frequency division multiple access signals on L1 and L2. However, the significant inconsistency between the phase bias of different ionospheric-free (IF) combinations for GLONASS-M+satellites, known as the phase inter-frequency clock bias (IFCB), hinders the utilization of GLONASS triple-frequency positioning. We discuss the coupling relationship between GLONASS IFCB and the phase center offset (PCO) and propose a new IFCB estimation model considering the PCO differences between L3 and L2. GLONASS triple-frequency observations from 151 globally distributed IGS stations are employed to validate the proposed IFCB estimation model. The results show that the mean root mean square (RMS) value of IFCB estimates decreases from 0.097 m to 0.028 m when considering PCO differences, suggesting the GLONASS IFCB is ignorable. Meanwhile, the L3 PCO estimates for GLONASS-M+satellites exhibit high stability and consistency, with standard deviations of 52, 113, and 13 mm, in *x*-, *y*-, and *z*-components, respectively. By correcting the estimated L3 PCO instead of the legacy IFCB, the GLONASS-only triple-frequency precise point positioning PPP achieves positioning accuracies of 1.8, 0.9, and 1.5 cm in east, north, and up components, with the improvement of 13%, 3%, and 33%, respectively. Moreover, the RMS value of L3 phase residuals reduces from 10.2 to 5.0 mm. Therefore, we recommend correcting the PCO on L3 for GLONASS-M+satellites and disregarding the IFCB for GLONASS triple-frequency positioning, which can significantly simplify the observation model and achieve higher accuracy.

Keywords GLONASS · Inter-frequency clock bias · Phase center offset · Triple-frequency precise point positioning · FDMA+CDMA

Introduction

As part of the GLONASS modernization program, the Russian satellite system commenced transmitting code division multiple access (CDMA) navigation signals on the third band L3 in 2011, in conjunction with the legacy frequency division multiple access (FDMA) signals on L1 and L2 (Urlichich et al. 2011). As of February 2023, the GLONASS constellation comprises 24 operational satellites distributed across three orbital slots, consisting of 15 GLONASS-M satellites, six GLONASS-M+satellites, and three GLONASS-K satellites. All GLONASS-M+(R04, R05, R12, R15, R21, and R24) and GLONASS-K satellites (R09, R11, and R22) are capable of transmitting the up-to-date L3 signals (Montenbruck et al. 2017). Extensive research has demonstrated that multi-frequency observations can expedite the initialization process of Global Navigation Satellite System (GNSS) precise positioning significantly and enhance accuracy (Geng et al. 2013; Guo et al. 2016; Li et al. 2019, 2020). Accordingly, the additional L3 signal is anticipated to bolster the performance of GLONASS navigation and positioning.

Zaminpardaz et al. (2017, 2021) initially analyzed the GLONASS L3 signal and discovered that the new CDMA data has a lower noise level than that of GPS, and evaluated the triple-frequency GLONASS RTK performance using the FDMA+CDMA-integrated model, successfully achieving

✉ Yongqiang Yuan
yqyuan@sgg.whu.edu.cn

1 School of Geodesy and Geomatics, Wuhan University, 129 Luoyu Road, Wuhan 430079, China

2 Hubei Luojia Laboratory, 129 Louyu Road, Wuhan 430079, China

double-differenced ambiguity resolution for a short baseline. However, in undifferenced triple-frequency GNSS data processing, such as precise point positioning (PPP), it is crucial to correct the inter-frequency clock bias (IFCB), caused by inconsistent and time-varying phase hardware delays between L1, L2, and L3. A lot of previous studies have reported that GPS Block IIF satellites suffer from severe IFCB, with inter-day amplitudes of up to 0.2 m (Montenbruck et al. 2010; Li et al. 2013; Pan et al. 2017). Zhang et al. (2022) estimated the IFCB of GLONASS using the same method applied to GPS, based on epoch-differenced geometry-free and ionospheric-free (GFIF) observations, and demonstrated that the IFCBs of GLONASS-K satellites are smaller than 0.01 m, while those of GLONASS-M + satellites reach 0.3 m. By correcting the estimated IFCB products, Zhang et al. (2023) accomplished GLONASS CDMA + FDMA-integrated PPP.

However, owing to the differences in the characteristics of the satellite, orbit, and navigation signals between GPS and GLONASS, the GPS IFCB estimation method is not fully applicable to GLONASS satellites. GLONASS IFCB results derived from the legacy GPS estimation method are irregular and difficult to model, and experiments of GLONASS triple-frequency positioning are currently limited to regional stations or short baselines. Moreover, we observe that the IFCB time series are significantly different from each other between stations with large distances. One of the possible reasons is that the effect of satellite antenna phase center offsets (PCOs) has been overlooked in previous IFCB estimation models, which are different for L1, L2, and L3 signals. Although the time-varying part of PCO differences in the radial component is ignorable for IFCB estimation due to the small variations of the satellite nadir angle, the horizontal PCO differences change dramatically with the azimuth angle (Schmid et al. 2005). Currently, neither the GPS nor the GLONASS PCO at third frequencies is provided in the IGS antenna model. Zeng et al. (2021) demonstrated that the differences between GPS L5 and L2 PCOs are 0.2, 0.1, and 9.9 cm, in the along-track, cross-track, and radial components, respectively. Small horizontal PCO differences for GPS Block IIF satellites mean that the impact of PCO differences can be ignored in GPS IFCB estimation. In contrast, we found that the horizontal PCO differences for GLONASS-M + satellites can reach 0.7 m, which can lead to decimeter-level and time-varying errors. Therefore, the PCO differences must be considered and carefully separated in GLONASS IFCB estimation.

In this contribution, we proposed a least-squared adjustment method to simultaneously estimate satellite phase IFCBs and PCO differences using GFIF observations derived from a reference network. Triple-frequency observations from 151 stations are utilized to estimate GLONASS IFCB and validate the proposed model. The characteristics of GLONASS IFCB, decoupled from PCO differences, are revealed and analyzed.

The GLONASS IFCB estimation model is demonstrated first. Then, we introduce the data and processing strategies, present the experimental validation of the GLONASS-only triple-frequency PPP, and, finally, the conclusions.

Method

We start with the GLONASS raw triple-frequency observation model. Then, we develop an FDMA + CDMA uncombined and undifferenced positioning model. Subsequently, we present a new GLONASS IFCB estimation method that accounts for the PCO differences on the L3 signal.

GLONASS triple-frequency observation model

Raw GLONASS observations of pseudorange P and carrier phase L can be expressed in units of meter as follows,

$$\begin{cases} P_{\mathrm{r},n}^{\mathrm{s}} = \rho_{\mathrm{r}}^{\mathrm{s}} + t_{\mathrm{r}} - t^{\mathrm{s}} + \gamma_n \cdot I_{\mathrm{r},1}^{\mathrm{s}} + T_r^s + b_{\mathrm{r},n}^{R_k} - b_n^s + e_{\mathrm{r},n}^s \\ L_{\mathrm{r},n}^{\mathrm{s}} = \rho_{\mathrm{r}}^{\mathrm{s}} + t_{\mathrm{r}} - t^{\mathrm{s}} - \gamma_n \cdot I_{\mathrm{r},1}^{\mathrm{s}} + T_{\mathrm{r}}^{\mathrm{s}} + \lambda_n^{R_k} \cdot N_{\mathrm{r},n}^s + B_{\mathrm{r},n}^{R_k} - B_n^s + \varepsilon_{\mathrm{r},n}^s \end{cases} \tag{1}$$

where s, r, n are the satellite, receiver, and frequency identifiers; R_k refers to the GLONASS channel number; $\rho_{\mathrm{r}}^{\mathrm{s}}$ is the geometric distance between the phase centers of satellite transmitter and receiver antenna; t_{r} and t^{s} denote the receiver and satellite clock offsets; f_{n,R_k} is the frequency, which are $f_{1,R_k} = 1602.0 + R_k \cdot 0.5625$ MHz, $f_{2,R_k} = 1246.0 + R_k \cdot 0.4375$ MHz, and $f_{3,R_k} = 1202.025$ MHz; the $I_{\mathrm{r},1}^{\mathrm{s}}$ refers to the slant ionospheric delay in L1; γ_n stands for the frequency-dependent multiplier factor, which is expressed as $\gamma_n = f_{1,R_k}^2 / f_{n,R_k}^2$; $T_{\mathrm{r}}^{\mathrm{s}}$ is the tropospheric delay;$\lambda_n^{R_k}$ denotes the wavelength of carrier phase; $N_{\mathrm{r},n}^s$ is the integer phase ambiguity in cycles; b and B refer to the hard- or software delays associated with code and phase measurements, respectively; $e_{\mathrm{r},n}^{\mathrm{s},R_k}$ and $\varepsilon_{\mathrm{r},n}^{\mathrm{s},R_k}$ are the sum of measurement noise and multipath errors.

For GLONASS FDMA L1 and L2 signals, the code and phase delays at the receiver end differ for satellites with different channel numbers. This leads to inconsistencies in receiver clock offsets, known as inter-frequency bias (IFB). Generally, the phase ambiguity can fully absorb IFB, whereas the code IFB is estimated as the difference relative to a particular satellite. Therefore, we reparametrize the raw observation equation and derive the GLONASS FDMA + CDMA PPP model as follows:

$$\begin{cases} P^{s}_{r,1} = \rho^{s}_{r} + \hat{t}^{R_0}_{r} - \hat{t}^{s} + \hat{I}^{s}_{r,1} + T^{s}_{r} + \mu^{R_k}_{r} + e^{s}_{r,1} \\ P^{s}_{r,2} = \rho^{s}_{r} + \hat{t}^{R_0}_{r} - \hat{t}^{s} + \gamma_2 \cdot \hat{I}^{s}_{r,1} + T^{s}_{r} + \mu^{R_k}_{r} + e^{s}_{r,2} \\ P^{s}_{r,3} = \rho^{s}_{r} + \hat{t}^{R_0}_{r} - \hat{t}^{s} + \gamma_3 \cdot \hat{I}^{s}_{r,1} + T^{s}_{r} + \omega^{s}_{r} + e^{s}_{r,3} \\ L^{s}_{r,1} = \rho^{s}_{r} + \hat{t}^{R_0}_{r} - \hat{t}^{s} - \hat{I}^{s}_{r,1} + T^{s}_{r} + \lambda^{R_k}_{1} \cdot \hat{N}^{s}_{r,1} + \varepsilon^{s}_{r,1} \\ L^{s}_{r,2} = \rho^{s}_{r} + \hat{t}^{R_0}_{r} - \hat{t}^{s} - \gamma_2 \cdot \hat{I}^{s}_{r,1} + T^{s}_{r} + \lambda^{R_k}_{2} \cdot \hat{N}^{s}_{r,2} + \varepsilon^{s}_{r,2} \\ L^{s}_{r,3} = \rho^{s}_{r} + \hat{t}^{R_0}_{r} - \hat{t}^{s} - \gamma_3 \cdot \hat{I}^{s}_{r,1} + T^{s}_{r} + \lambda_3 \cdot \hat{N}^{s}_{r,3} - \Theta^{s}_{UC} + \varepsilon^{s}_{r,2} \end{cases} \tag{2}$$

with

$$\begin{cases} \hat{t}^{s} = t^{s} + (\alpha^{R_k}_{12} b^{s}_{1} + \beta^{R_k}_{12} b^{s}_{2}) \\ \hat{t}^{R_0}_{r} = t_r + (\alpha^{R_k}_{12} b^{R_0}_{r,1} + \beta^{R_k}_{12} b^{R_0}_{r,2}) \\ \kappa^{s}_{r} = \beta^{R_k}_{12}(b^{R_k}_{r,1} - b^{R_k}_{r,2}) - \beta^{R_k}_{12}(b^{s}_{1} - b^{s}_{2}) \\ \hat{I}^{s}_{r,1} = I^{s}_{r,1} + \kappa^{s}_{r} \\ \mu^{R_k}_{r} = \alpha^{R_k}_{12} b^{R_k}_{r,1} + \beta^{R_k}_{12} b^{R_k}_{r,2} - (\alpha^{R_k}_{12} b^{R_0}_{r,1} + \beta^{R_k}_{12} b^{R_0}_{r,2}) \\ \omega^{s}_{r} = b_{r,3} - b^{s}_{3} - (\alpha^{R_k}_{12} b^{R_k}_{r,1} + \beta^{R_k}_{12} b^{R_k}_{r,2}) + (\alpha^{R_k}_{12} b^{s}_{1} + \beta^{R_k}_{12} b^{s}_{2}) - \gamma_3 \kappa^{s}_{r} \\ \hat{N}^{s}_{r,1} = N^{s}_{r,1} + B^{R_k}_{r,1} - B^{s}_{1} - (\alpha^{R_k}_{12} b^{R_0}_{r,1} + \beta^{R_k}_{12} b^{R_0}_{r,2})/\lambda^{R_k}_{1} + (\alpha^{R_k}_{12} b^{s}_{1} + \beta^{R_k}_{12} b^{s}_{2})/\lambda^{R_k}_{1} + \kappa^{s}_{r}/\lambda^{R_k}_{1} \\ \hat{N}^{s}_{r,2} = N^{s}_{r,2} + B^{R_k}_{r,2} - B^{s}_{2} - (\alpha^{R_k}_{12} b^{R_0}_{r,1} + \beta^{R_k}_{12} b^{R_0}_{r,2})/\lambda^{R_k}_{2} + (\alpha^{R_k}_{12} b^{s}_{1} + \beta^{R_k}_{12} b^{s}_{2})/\lambda^{R_k}_{2} + \gamma_2 \kappa^{s}_{r}/\lambda^{R_k}_{2} \\ \hat{N}^{s}_{r,3} = N^{s}_{r,3} + B_{r,3} - \overline{B}^{s}_{3} - (\alpha^{R_k}_{12} b^{R_0}_{r,1} + \beta^{R_k}_{12} b^{R_0}_{r,2})/\lambda_3 + (\alpha^{R_k}_{12} b^{s}_{1} + \beta^{R_k}_{12} b^{s}_{2})/\lambda_3 + \gamma_3 \kappa^{s}_{r}/\lambda_3 \\ \Theta^{s}_{UC} = B^{s}_{3} - \overline{B}^{s}_{3} \end{cases} \tag{3}$$

where $\hat{t}^{s}$ is the satellite clock offsets that absorbed the ionospheric-free (IF) combination satellite hardware delays, commonly correcting with IGS precise clock products; $\hat{t}^{R_0}_{r}$ denotes the receiver clock offsets that absorbed the IF combination receiver hardware delays of a reference satellite R_0; $\alpha^{R_k}_{12}$ and $\beta^{R_k}_{12}$ are coefficients of the IF combinations with $\alpha^{R_k}_{12} = f^2_{1,R_k}/(f^2_{1,R_k} - f^2_{2,R_k})$ and $\beta^{R_k}_{12} = -f^2_{2,R_k}/(f^2_{1,R_k} - f^2_{2,R_k})$; $\mu^{R_k}_{r}$ refers to the GLONASS IFB; ω^{s}_{r} is the third-frequency IFB, which have to be estimated for each receiver and satellite pair and can fully absorb the code IFCB (Li et al. 2018); $\overline{B}^{s}_{3}$ denote the constant part of B^{s}_{3} and can be absorbed into the phase ambiguity $\hat{N}^{s}_{r,3}$, while the time-varying part Θ^{s}_{UC} is the phase IFCB of the uncombined model. Pan et al. (2019) proved that the conversion between Θ^{s}_{UC} and the IF combination phase IFCB Θ^{s}_{IF} derived from GFIF observations is $\Theta^{s}_{UC} = \frac{f^2_{1,R_k} - f^2_3}{f^2_3} \cdot \Theta^{s}_{IF}$.

GLONASS IFCB estimation method

GFIF observations are commonly used for IFCB estimation (Pan et al. 2017; Zhang et al. 2022). By taking the difference between the IF combination phase observations of L1/L2 and L1/L3, the geometric distance, clock offsets, first-order ionospheric delay, and tropospheric delay can be eliminated. Hence, the GFIF observation $L^{s}_{r,GFIF}$ can be represented as the sum of the constant phase ambiguity, the time-varying IFCB, and the time-varying PCO errors in the line-of-sight direction:

$$\begin{aligned} L^{s}_{r,GFIF} &= L^{s}_{r,IF12} - L^{s}_{r,IF13} \\ &= \hat{N}^{s}_{r,GFIF} + \Theta^{s}_{IF} + \mathbf{u}^{s}_{r} \cdot \mathbf{\Phi}^{s} \cdot \mathbf{r}^{s,PCO}_{GFIF} + \varepsilon^{s}_{r,GFIF} \end{aligned} \tag{4}$$

with

$$\begin{cases} \hat{N}^{s}_{r,GFIF} = N^{s}_{r,IF12} - N^{s}_{r,IF13} + (\alpha_{12}B_{r,1} + \beta_{12}B_{r,2}) - (\alpha_{13}B_{r,1} + \beta_{13}B_{r,3}) \\ \quad + (\alpha_{12}B^{s}_{1} + \beta_{12}B^{s}_{2}) - (\alpha_{13}B^{s}_{1} + \beta_{13}\overline{B}^{s}_{3}) \\ \Theta^{s}_{IF} = -\beta_{13} \cdot (B_3 - \overline{B}_3) \\ \mathbf{r}^{s,PCO}_{GFIF} = \mathbf{r}^{s,PCO}_{IF12} - \mathbf{r}^{s,PCO}_{IF13} \end{cases} \tag{5}$$

where $\hat{N}^{s}_{r,GFIF}$ is the linear combination of phase ambiguities and the constant parts of phase hardware delays; Θ^{s}_{IF} denote the IF combination IFCB; $\mathbf{r}^{s,PCO}$ stands for the vector of satellite PCO correction in the satellite-fixed coordinate system, where the *z*-axis points to the Earth, the *y*-axis is the rotation axis of solar panel and *x*-axis follows the right-handed system (Schmid et al. 2005); $\mathbf{\Phi}^{s}$ is the rotation matrix from satellite-fixed frame to ITRF, which can be obtained from IGS satellite attitude products; $\mathbf{u}^{s}_{r}$ is the line-of-sight unit vector in ITRF; $\varepsilon^{s}_{r,GFIF}$ is the sum of measurement noise, multipath errors, and high-order ionospheric delays. It was reported that the time-varying part of receiver IFCB is small enough to be ignored (Li et al. 2012). Therefore, we focus on the satellite IFCB in this contribution.

Then, the constant part $\hat{N}^{s}_{r,GFIF}$ in GFIF observation can be eliminated by the epoch difference (ED) approach:

$$\begin{aligned}\Delta L^{s}_{r,GFIF}(t,t-1) &= L^{s}_{r,GFIF}(t) - L^{s}_{r,GFIF}(t-1)\\ &= \Delta\Theta^{s}(t,t-1) + \Delta\mathbf{w}^{s}_{r}(t,t-1)\cdot\mathbf{r}^{s,PCO}_{GFIF}\end{aligned} \tag{6}$$

where $\Delta\Theta^{s}(t,t-1)$ denotes the ED IFCB; $\mathbf{w}^{s}_{r}$ refers to the line-of-sight unit vector in the satellite-fixed coordinate system, which is expressed as $\mathbf{w}^{s}_{r} = [w_x, w_y, w_z]$; therefore, $\Delta\mathbf{w}^{s}_{r}(t,t-1)$ can be expressed as $\Delta\mathbf{w}^{s}_{r} = [\Delta w_x(t,t-1), \Delta w_y(t,t-1), \Delta w_z(t,t-1)]$. Considering the standard deviation (STD) of GFIF observation is $\sigma_{GFIF} = \sqrt{(\alpha_{12}^2 - \alpha_{13}^2)\sigma_{L1}^2 + \beta_{12}^2\sigma_{L2}^2 + \beta_{13}^2\sigma_{L3}^2}$, the STD of $\Delta\Theta^{s}(t,t-1)$ can be expressed as $\sigma_{\Delta\Theta^s} = \sqrt{2}\sigma_{GFIF}$, where σ_{L1}, σ_{L2}, and σ_{L3} are all set as 0.02 cycle (Zaminparda et al. 2017). For quality control, ED GFIF observations that are larger than $3\sigma_{\Delta\Theta^s}$ are removed (Zhang et al. 2022). Hence, we can set up a least-square adjustment for each satellite using ED GFIF from a reference network, and the estimated parameters are:

$$\mathbf{x} = [r^{s,PCO}_{GFIF,x}, r^{s,PCO}_{GFIF,y}, r^{s,PCO}_{GFIF,z}, \Delta\Theta^{s}(t_1,t_0), \Delta\Theta^{s}(t_2,t_1), \cdots, \Delta\Theta^{s}(t_n,t_{n-1})] \tag{7}$$

Afterward, the IFCB value at an arbitrary epoch t_n can be computed by the IFCB value at the reference epoch and ED IFCB values:

$$\Theta^{s}(t_n) = \Theta^{s}(t_0) + \sum_{i=1}^{n}\Delta\Theta^{s}(t_i,t_{i-1}) \tag{8}$$

where $\Theta^{s}(t_0)$ can be set to an arbitrary value because it can be absorbed in phase ambiguities in parameter estimation.

Here, we set a zero-mean constraint for all IFCB values to guarantee the continuity of adjacent daily solutions, with

$$\Theta^{s}(t_0) = \sum_{i=1}^{n}(i-n)\cdot\Delta\Theta^{s}(t_i,t_{i-1}) \tag{9}$$

Meanwhile, the satellite L3 PCO ($\mathbf{r}^{s,PCO}_{3}$) can be derived from the GFIF PCO estimates ($\mathbf{r}^{s,PCO}_{GFIF}$) through the following equation:

$$\mathbf{r}^{s,PCO}_{3} = \left[(\alpha_{12}-\alpha_{13})\cdot\mathbf{r}^{s,PCO}_{1} + \beta_{12}\cdot\mathbf{r}^{s,PCO}_{2} - \mathbf{r}^{s,PCO}_{GFIF}\right]/\beta_{13} \tag{10}$$

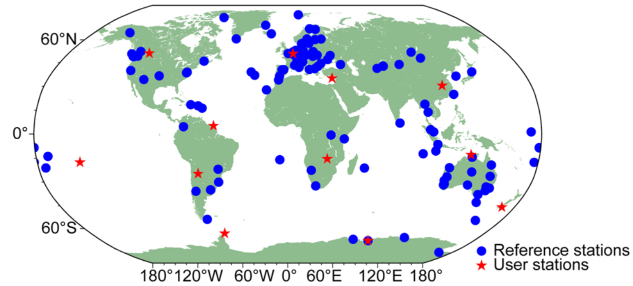

Fig. 1 Distribution of IGS stations used for the GLONASS IFCB estimation (blue cycles) and triple-frequency PPP validation (red pentagrams)

where $\mathbf{r}^{s,PCO}_{3}$ and $\mathbf{r}^{s,PCO}_{3}$ refer to the satellite PCO of L1 and L2. And the STD of $\mathbf{r}^{s,PCO}_{3}$ can be computed by $\sigma_{\mathbf{r}^{s,PCO}_{3}} = \sigma_{\mathbf{r}^{s,PCO}_{GFIF}}/\beta_{13}$.

Data and processing strategy

As of February 2023, nine operational GLONASS satellites are transmitting L3 navigation signals, including six GLONASS-M + satellites (R04, R05, R12, R15, R21, and R24) and three GLONASS-K satellites (R09, R11, and R22). We collect the GLONASS triple-frequency observations for 100 days in DOY 210–310, 2022 to estimate the GLONASS IFCB and evaluate the performance of GLONASS-only triple-frequency PPP. Figure 1 shows the distribution of the GLONASS reference network and user stations. We use 151 IGS stations in blue cycles for IFCB estimation and eight user stations in red pentagrams for GLONASS triple-frequency PPP. In addition, the precise GNSS orbit and attitude quaternion products from the German Research Center for Geosciences (GFZ) are utilized in IFCB estimation.

Table 1 summarizes the processing strategy of GLONASS triple-frequency PPP. We utilize the undifferenced and uncombined PPP model. GLONASS IFBs are estimated as constant values for each satellite, and the third-frequency IFBs are estimated as the random walk for each station-satellite pair. In this contribution, the GREAT (GNSS + Research, Application, and Teaching) software developed by Wuhan University was employed to handle the IFCB estimation and multi-frequency PPP (Li et al. 2021).

Table 1 Processing strategy of GLONASS triple-frequency PPP

Items	Models
Observations	Undifferenced and uncombined code and phase observations
Sampling interval	30 s
Weighting	Elevation-dependent weighting with a 7° cutoff
Satellite antenna model	L1 and L2: use values from igs14.atx; L3: use the estimated values
Receiver antenna model	L1 and L2: use values from igs14.atx; L3: use values of L2
Satellite orbits and clocks	GFZ precise products
Tropospheric delay	Priori delay by Saastamoinen model (Saastamoinen 1973) with Global Mapping Function (Boehm et al. 2006); estimating zenith troposphere delays (ZTDs) as piecewise constants every 2 h
Ionospheric delay	Estimated as the random walk
Phase ambiguity	Constant over each continuous observation arc
Receiver clock offset	Estimated as white noise; estimate IFB for each GLONASS satellite as constants; estimate the third-frequency IFB for each satellite-receiver pair as the random walk

Table 2 Detailed information of the six stations used in single-receiver IFCB estimation

Group	Station	Receiver	Antenna	Lon [deg]	Lat [deg]
A	FFMJ	JAVAD TRE_3 DELTA	LEIAR25.R3 LEIT	8.665	50.091
	GANP	SEPT POLARX5TR	JAVRINGANT_DM	20.323	49.035
	GOP6	SEPT POLARX5	SEPCHOKE_B3E6	14.786	49.914
B	MAC1	SEPT POLARX5	JAVRINGANT_DM	158.936	−54.500
	MOBS	SEPT POLARX5	JAVRINGANT_DM	144.975	−37.829
	TUVA	SEPT POLARX5	JAVRINGANT_DM	179.197	−8.525

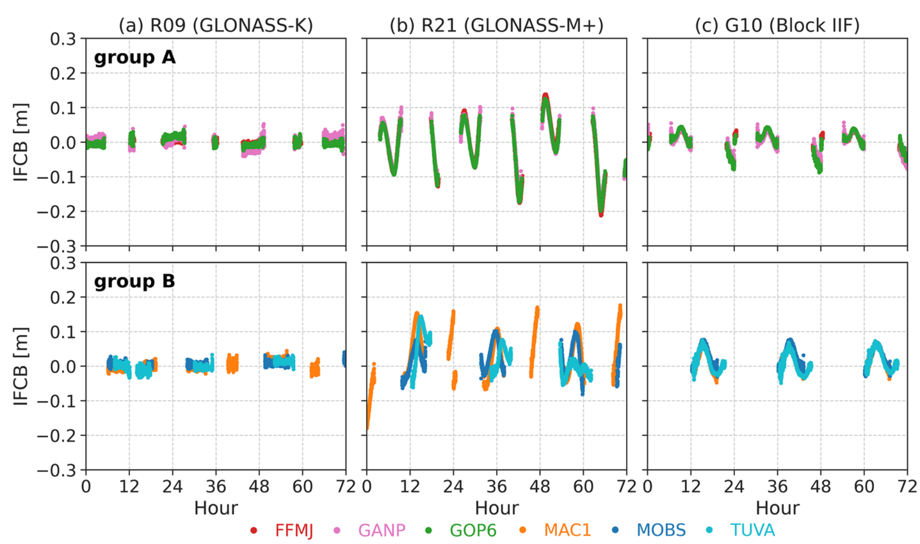

Fig. 2 Single-receiver IFCB results for R09, R21, and G10 (from the left column to the right) in DOY 215–217, 2022. Six stations are divided into group A and group B with their results showing in the first and second rows

Validation experiment

First, the single-receiver IFCB results are investigated to illustrate the coupling relationship between IFCB and PCO. Next, we perform the IFCB estimation with the new method, evaluate the IFCB results, analyze the PCO estimations, and provide an L3 PCO correction for GLONASS-M + satellites. Finally, we implement the GLONASS-only triple-frequency PPP using the estimated PCO corrections.

Analysis of single-receiver IFCB results

Six IGS stations are selected and categorized into two groups, i.e., A and B, with their detailed information listed in Table 2. Three stations in group A are equipped with different receivers and antennas, although their distances are relatively close (41 to 83 km). In contrast, the three stations in group B are outfitted with identical receivers and antennas, but their distances are very far (211 to 539 km).

Figure 2 depicts the IFCB time series of R09 (GLONASS-K), R21 (GLONASS-M+), and G10 (Block IIF, for comparison) obtained from the six selected stations in DOY 215–217, 2022. Notably, the time series of R09 exhibit minimal variation, with a scatter of less than 0.05 m, and demonstrate exceptional consistency across all six stations. Similar consistency can also be found for G10, albeit fluctuating over time. These findings suggest that the IFCB estimates of GLONASS-K and GPS Block IIF satellites are solely satellite-dependent and are not influenced by the type of receiver, antenna, or station location, as reported in previous studies (Pan et al. 2017; Zhang et al. 2022). However, this phenomenon is not observed for R21, as evidenced by the significant differences in the three IFCB time series from group B with intersecting fluctuations.

In contrast, the R21 IFCB results from group A exhibit a high degree of similarity. This observation leads to the inference that the IFCB estimates of R21 are affected by the station location rather than the receiver type or antenna. Additionally, it is worth noting that the IFCB time series of each continuous observation arc exhibit V-shaped or invert-V-shaped patterns, indicating a possible association with the azimuth and the nadir of the satellite signals. We can further deduce that the inconsistency in the R21 IFCB estimates is due to the difference in satellite PCOs of L2 and L3.

Figure 3 presents the time series of R21 IFCB in DOY 215–217 of 2022, and the line-of-sight unit vector in the *x*-, *y*-, and *z*-components in the satellite-fixed frame; these are also the coefficients of *x*-, *y*-, and *z*-offset in (7). It is observed that the variations of the *z*-coefficient, i.e., the cosine of nadir, are minimal (0.97–0.99), whereas the peak-to-peak value of IFCB is approximately 0.2 m. Assuming that the *z*-offset error causes the fluctuations of IFCB, the *z*-offset error would have to be up to 10 m, which is highly improbable. On the other hand, the variation of the *y*-coefficient is significant; however, the time series of the *y*-coefficient does not follow the V-shaped or invert-V-shaped patterns like IFCB. In contrast, the shape of the time series of the *x*-coefficient is strikingly similar to that of the IFCB, and the peak-to-peak value of the *x*-coefficient reaches 0.3, suggesting that the *x*-offset is the main cause of the fluctuations of IFCB estimates.

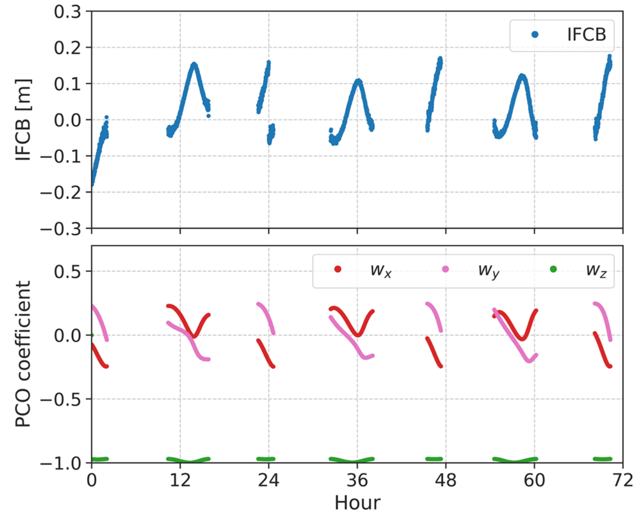

Fig. 3 Time series of R21 IFCB derived from MAC1 (upper) in DOY 215–217, 2022, and the line-of-sight unit vector $\mathbf{w} = [w_x, w_y, w_z]$ in the satellite-fixed coordinate system (bottom)

To elucidate the connection between IFCB and *x*-offset, we present a scatter diagram of R21 IFCB estimates and the coefficients of *x*-offset in Fig. 4. As can be observed, all IFCB outcomes from the six stations exhibit linear correlations with the *x*-coefficient, with similar slopes of approximately − 0.7. These results further confirm the hypothesis that the *x*-offset of R21 is responsible for the inconsistency in the IFCB estimates.

GLONASS IFCB results considering the PCO differences

Based on the above analysis, the IFCB estimation considering PCO differences is performed for GLONASS-M + satellites using the proposed method. Figure 5 illustrates the GLONASS IFCB results obtained from 151 globally distributed stations on DOY 295, 2022. Additionally, the results of three GLONASS-K satellites (R09, R11, and R22) are included for comparison purposes. Intraday IFCB time series of GLONASS-K satellites exhibit very small variation, while the IFCB time series of GLONASS-M + satellites without PCO corrections display severe and precipitous fluctuations, consistent with previous findings (Zhang et al. 2023). In contrast, the IFCB results considering PCO differences exhibit values around zero with peak-to-peak values smaller than 0.05 m, indicating that the true IFCB of GLONASS-M + is very small when the influence of PCO differences is eliminated. It should be noted that the IFCB time series of R15 is intermittent, as only 33 stations are tracking the signal of R15.

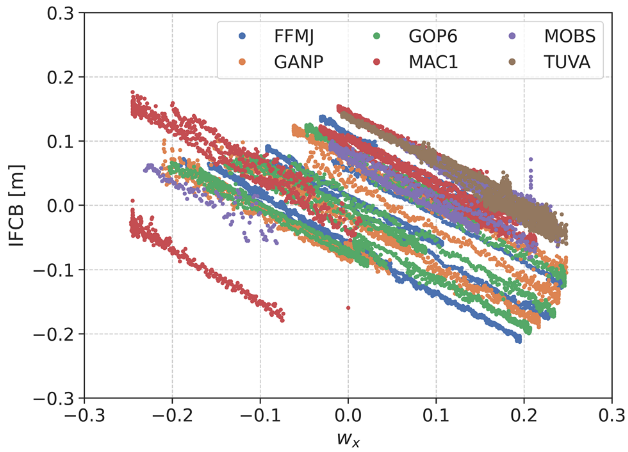

Fig. 4 Scatter diagram of the R21 IFCB values derived from the six stations in DOY 215–217, 2022 vs. the corresponding coefficients of *x*-offset

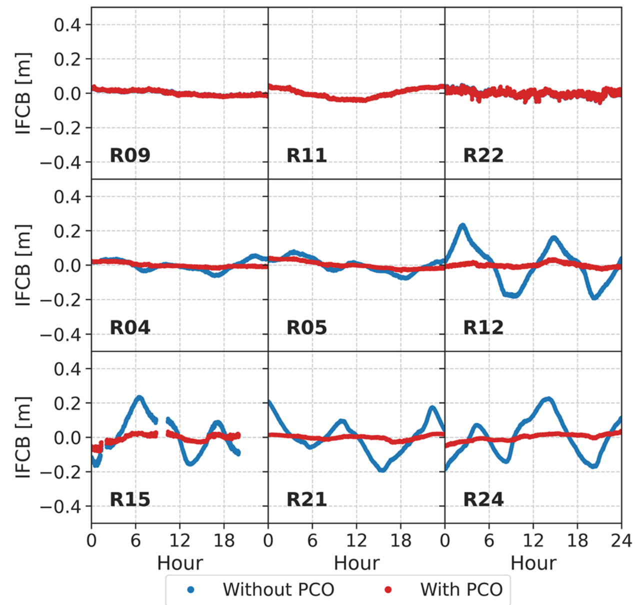

Fig. 5 IFCB time series for GLONASS-K and GLONASS-M + satellites derived from 151 stations on DOY 295, 2022

To further investigate the inter-day characteristics of GLONASS IFCB, we have depicted the IFCB time series for 100 days in Fig. 6. The results of GLONASS-K satellites are also included for comparison purposes. As can be observed, the IFCB time series derived without PCO correction exhibit both a medium-term variation of approximately 8 days and a long-term variation that varies with the orbital planes. The medium-term variation can be attributed to the orbit parameters of GLONASS satellites, which have a period of revolution of 11 h,15 m,44 s, and a ground track repeat cycle of 8 days. Furthermore, the IFCB time-series amplitude changes with the sun's elevation to the orbital plane, i.e., the beta angle. As the absolute value of the beta angle increases, the amplitude decreases slowly and smoothly. Notably, the *y*-axis of the satellite-fixed coordinate system corresponds to the rotation axis of the solar panel, which is associated with the beta angle.

Consequently, the satellite attitude changes with the beta angle, leading to the variation of the PCO differences in GFIF observations. Conversely, the IFCB time series considering PCO differences, exhibit excellent stability and concentrate around zero. This phenomenon serves as further evidence that the PCO differences in IFCBs have been successfully separated, and the resulting clean IFCBs can be obtained.

Then, we summarize the root mean square (RMS) values of 100-day IFCB estimates of GLONASS-M + satellites, as depicted in Fig. 7. By separating the PCO errors from GFIF observations, the mean RMS value of IFCB estimates decreases from 0.097 m to 0.028 m, with an improvement of 71%. Moreover, all GLONASS-M + satellites, except satellite R15, exhibit RMS values of less than 0.03 m and mean values of less than 1e-8 m. The remaining IFCB can be attributed to the observation noise, higher-order ionospheric delays, or other unmodeled errors. Based on these findings, we recommend that the IFCB of GLONASS-M + satellites can be disregarded if the correct satellite PCO is applied for the L3 signal.

GLONASS PCO results

In this section, we evaluate the accuracy of PCO derived from the GFIF observations of 151 IGS stations and present the final L3 PCO estimates for GLONASS-M + satellites. Figure 8 illustrates the *x*-offset, *y*-offset, and *z*-offset estimates for GLONASS-M + satellites from DOY 210 to DOY 310 in 2022. We observe that the *x*-offset estimates for all satellites exhibit excellent stability and converge to approximately -0.7 m. The *z*-offset estimates are nearly zero, which may reflect the low sensitivity of ED GFIF observations to *z*-offsets. The *y*-offset estimates demonstrate relatively less stability than the *x*- and *z*-offsets, particularly for R05 in DOY 210–220, R12 in DOY 300–310, and R21/R24 in DOY 275–285. This may stem from the error of the satellite attitude model during the low beta angle. R15 PCO estimates are erratic owing to the scarce tracking stations of R15 during the experimental period.

IGS antenna model has provided the IF(1, 2) combination PCO for GLONASS-M + satellites, which is (-545.00, 0.00, 2450.00) mm, and is used for the L1 and L2 PCO in this study. Then, the L3 PCO estimates can be derived from GFIF PCO estimates as (11). Table 3 presents the L3 PCO estimates and their corresponding STDs for GLONASS-M + satellites. The R15 computation employs only data from

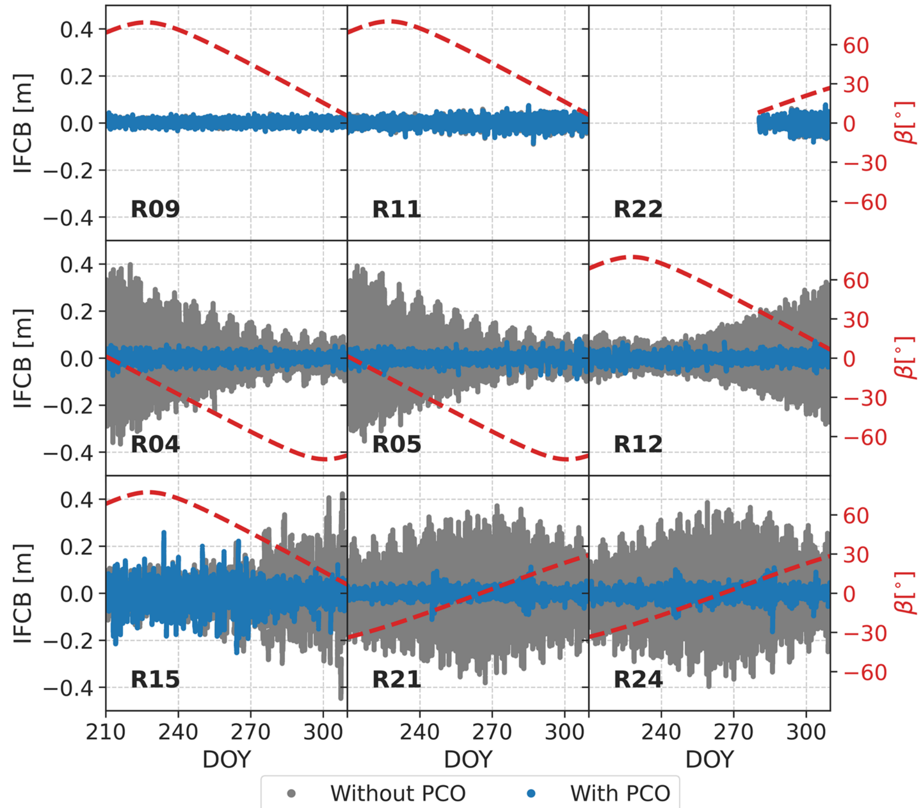

Fig. 6 IFCB time series for GLONASS-K and GLONASS-M+satellites from DOY 210 to DOY 310 in 2022. Red lines refer to the sun's elevation to the orbital plane, i.e., the beta angle

DOY 275–310 due to poor estimates during the initial days. Mean STD values for *x*-, *y*-, and *z*-offsets are 52, 113, and 13 mm, respectively, which suggests that the PCO estimates exhibit high accuracy. Notably, no significant differences exist among the PCO estimates of GLONASS-M+satellites, particularly in the *x*- and *z*-components, with maximum differences of 7.6 and 16.1 mm. Therefore, the final L3 PCO estimates for GLONASS-M+satellites can be obtained by averaging the weighted values of all satellites except R15, which is (−1072.39, 152.94, 2425.01) mm. However, the x-offset appears deviant, as it even reaches 1 m. This is due to the fact that the obtained L3 PCO is a relative value against the PCO of L1 and L2. In this study, we derive the L3 PCO from the IF(1, 3) PCO, which is (131.89, -195.94, 2482.09) mm, where the L1 and L2 PCOs are fixed to the value of IF(1, 2). The uncombined L3 PCO correction for each frequency requires further investigation.

GLONASS-only triple-frequency PPP

To validate the estimated L3 PCO for GLONASS-M+satellites, we design three strategies to perform the GLONASS-only triple-frequency PPP as follows: **S1**: use the L2 PCO corrections from igs14.atx for L3 and no IFCB correction; **S2**: use the L2 PCO corrections from igs14.atx for L3 and use IFCB correction derived from the standard model; **S3**: use the estimated L3 PCO and no IFCB correction.

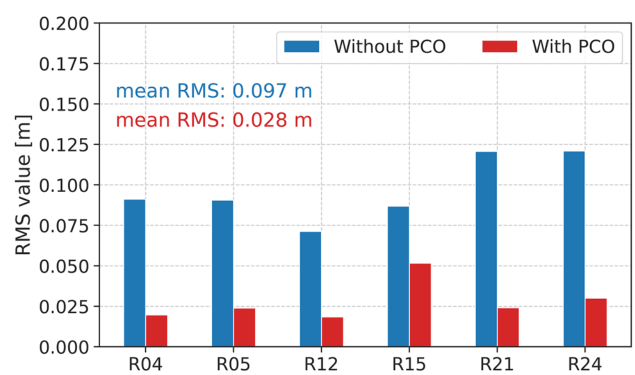

Fig. 7 RMS values of the IFCB estimates for GLONASS-M+satellites from DOY 210 to DOY 310 in 2022

Raw triple-frequency GLONASS data from eight global-distributed stations (as shown in Fig. 1) on DOY 295, 2022 are employed for the PPP. Figure 9 illustrates the positioning errors of BRUX, MIZU, and NICO under the three strategies. It is observed that S1 suffers from a bias of up to 0.2 m due to the inappropriate L3 PCO corrections. By applying the IFCB correction from the standard model, S2 partially mitigates the positioning errors. However, the PCO differences are not eliminated by the IFCB correction, and the performance differs depending on the station's geographic

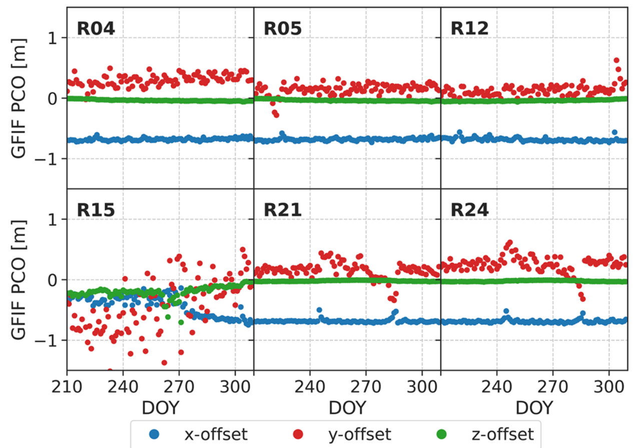

Fig. 8 Time series of *x*-offset (blue), *y*-offset (red), and *z*-offset (green) estimates for GLONASS-M + satellites from DOY 210 to DOY 310 in 2022

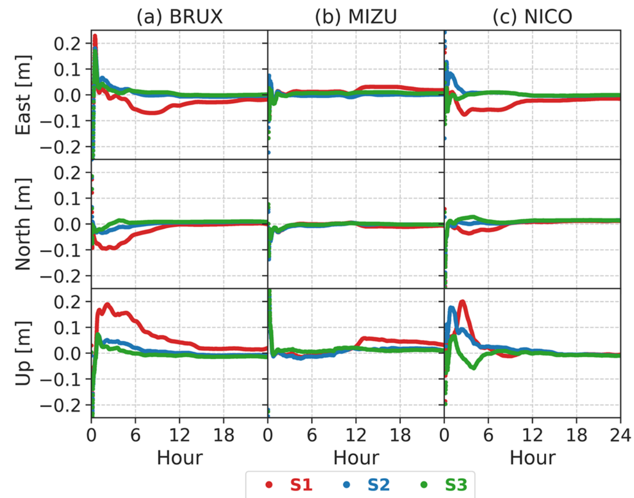

Fig. 9 Positioning errors of GLONASS-only triple-frequency PPP for BRUX **a**, MIZU **b**, and NICO **c** on DOY 295, 2022

Table 3 L3 PCO estimates and STDs for GLONASS-M + satellites (unit: mm)

Satellite	*x*-offset	*y*-offset	*z*-offset	STD-*x*	STD-*y*	STD-*z*
R04	– 1073.37	232.84	2421.88	51	78	10
R05	– 1069.12	113.16	2422.00	52	73	10
R12	– 1070.31	96.81	2418.66	59	75	9
R15	– 1035.17	-101.51	2361.71	45	231	35
R21	– 1073.38	118.59	2434.73	59	108	6
R24	– 1076.75	194.50	2432.77	43	111	7

location. In contrast, S3 exhibits the best positioning accuracy and convergence time, suggesting the high accuracy of the estimated L3 PCO.

Figure 10 depicts the RMS values of the positioning errors for the eight stations. First-hour results during the convergence time are excluded. As can be observed, the S3 strategy manifests the most elevated accuracy in the east, north, and up components, with average RMS values of 1.8, 0.9, and 1.5 cm. In comparison to the outcomes of S2, the positioning errors are reduced by 13%, 3%, and 33% in the three components. Moreover, the improvement in NICO and ZAMB in the up component exceeds 50%.

We also examined the phase residuals for the three strategies, as shown in Fig. 11. RMS values of L3 residuals for S1 range from 10 to 16 mm, while those of S2 exhibit a more drastic variation from 4 to 18 mm, indicating that the IFCB from standard model fails to model the extra bias in L3 phase observation properly. In contrast, the RMS values of L3 residuals for S3 are consistently around 5 mm, with an improvement of 51% compared with those of S2.

Conclusions

Modernization of GLONASS has led to six GLONASS-M + and three GLONASS-K operational satellites transmitting the new CDMA signal at the third frequency and the legacy FDMA signals L1 and L2. However, the presence of extra phase bias on GLONASS L3 observations, previously known as IFCB, hinders the application of GLONASS triple-frequency positioning. In this study, we investigate the characteristics of the GLONASS IFCB estimates derived from single-receiver GFIF observations. The GLONASS-M + satellite IFCBs estimated by stations that are located far apart exhibit significant discrepancies, whereas they are highly consistent for nearby stations. Then, we demonstrate that the single-receiver IFCB estimates of GLONASS-M + satellites are independent of receiver or antenna type and are solely influenced by the relative position between the satellite and the receiver. Furthermore, we discover that the IFCB estimates of GLONASS-M + satellites demonstrate a notable linear correlation with the satellite PCO in the *x*-component of the satellite-fixed coordinate system.

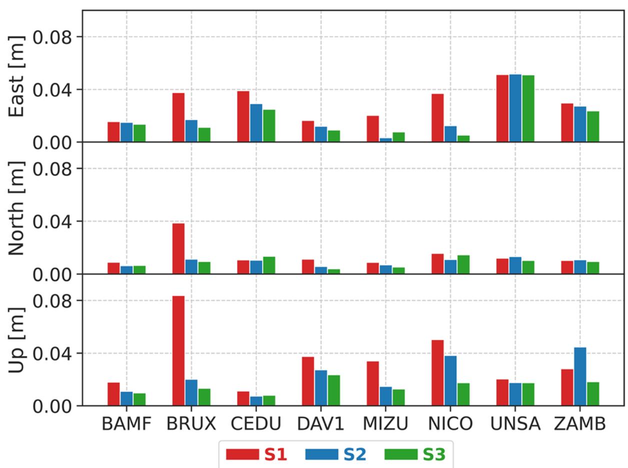

Fig. 10 RMS values of the positioning errors of GLONASS-only triple-frequency PPP for the selected stations on DOY 295, 2022. First-hour results during the convergence time are excluded

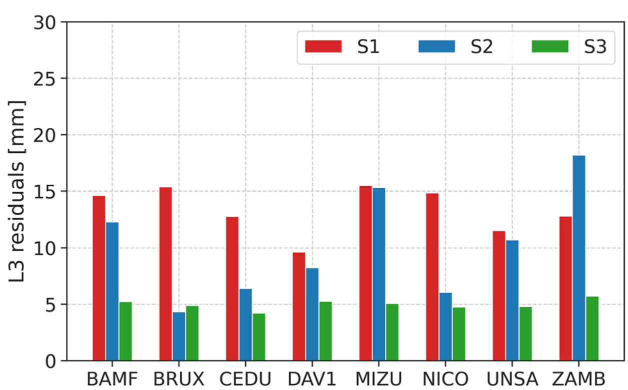

Fig. 11 RMS values of L3 residuals in PPP for the selected stations on DOY 295, 2022

Based on the analysis of GLONASS IFCB, we propose a modified IFCB estimation model that simultaneously estimates GFIF PCOs and IFCBs. GLONASS triple-frequency observations from 151 globally distributed IGS stations are utilized for the IFCB estimation. We analyze both the intraday and inter-day characteristics of the IFCB estimates derived from these 151 stations. The results show that the IFCB time series considering PCO differences exhibit minimal variation, with the mean RMS value decreasing from 0.097 m to 0.028 m. The performance of the IFCB estimates suggests that the majority of the extra phase bias in L3 is caused by the PCO differences rather than the GPS-like IFCB. Therefore, the IFCB can be ignored in GLONASS triple-frequency data processing if only the L3 PCO is precisely corrected.

Hence, we evaluate the accuracy of the estimated PCO for GLONASS-M + satellites. The estimated *x*-, *y*-, and *z*-offsets for each satellite exhibit high stability and consistency, with mean STD values of 52, 113, and 13 mm, respectively. Therefore, we obtain the final L3 PCO corrections for GLONASS-M + satellites by averaging the weighted values of PCO estimates for each satellite, which equates to (-1072.39, 152.94, 2425.01) mm. With the precise L3 PCO correction, we carry out the GLONASS-only triple-frequency PPP using the uncombined and undifferenced observation model. Raw triple-frequency GLONASS data from eight globally distributed stations on DOY 295, 2022 are employed for the PPP. By comparing the new strategy that employs the estimated L3 PCO value and ignores IFCB with the traditional strategy that utilizes the L2 PCO value for L3 and corrects the IFCB, we observe a significant improvement in positioning accuracy. Specifically, the new strategy results in an improvement of 13%, 3%, and 33% in the east, north, and up components, respectively. Moreover, the RMS value of L3 phase residuals reduces from 10.2 to 5.0 mm, further validating that the new strategy has appropriately modeled the extra bias on GLONASS L3.

Acknowledgements This study is financially supported by the National Natural Science Foundation of China (No. 41974027, No. 42204017), the Hubei Province Natural Science Foundation (Grant No. 2020CFA002), the special fund of Hubei Luojia Laboratory (220100006), the Fundamental Research Funds for the Central Universities (2042022kf1001), and the Sino-German mobility program (Grant No. M-0054). The numerical calculations in this paper have been done on the supercomputing system in the Supercomputing Center of Wuhan University.

Author contributions JW and XL provided the initial idea and designed the experiments for this study; JW, XL, YY, and XL analyzed the data and wrote the manuscript; XL, HZ, and WZ helped with the writing. All authors reviewed the manuscript.

Data availability All data in this article are publicly accessible. The GNSS data and products can be obtained at https://cddis.nasa.gov/archive.

Declarations

Competing interests The authors declare no competing interests.

References

Boehm J, Niell A, Tregoning P, Schuh H (2006) Global mapping function (GMF): a new empirical mapping function based on numerical weather model data. Geophys Res Lett. https://doi.org/10.1029/2005gl025546

Geng J, Bock Y (2013) Triple-frequency GPS precise point positioning with rapid ambiguity resolution. J Geod 87(5):449–460. https://doi.org/10.1007/s00190-013-0619-2

Guo F, Zhang X, Wang J, Ren X (2016) Modeling and assessment of triple-frequency BDS precise point positioning. J Geod 90(11):1–13

Li H, Zhou X, Wu B, Wang J (2012) Estimation of the inter-frequency clock bias for the satellites of PRN25 and PRN01. Sci China Phys, Mech Astron 55(11):2186–2193
Li H, Zhou X, Wu B (2013) Fast estimation and analysis of the inter-frequency clock bias for Block IIF satellites. GPS Solut 17(3):347–355. https://doi.org/10.1007/s10291-012-0283-7
Li P, Zhang X, Ge M, Schuh H (2018) Three-frequency BDS precise point positioning ambiguity resolution based on raw observables. J Geod 92:1357–1369
Li X, Li X, Liu G, Feng G, Yuan Y, Zhang K, Ren X (2019) Triple-frequency PPP ambiguity resolution with multi-constellation GNSS: BDS and Galileo. J Geod 93:1105–1122
Li X, Liu G, Li X, Zhou F, Feng G, Yuan Y, Zhang K (2020) Galileo PPP rapid ambiguity resolution with five-frequency observations. GPS Solut 24:1–13
Li X, Han X, Li X, Liu G, Feng G, Wang B, Zheng H (2021) GREAT-UPD: an open-source software for uncalibrated phase delay estimation based on multi-GNSS and multi-frequency observations. GPS Solut 25(2):1–9
Montenbruck O, Steigenberger P, Prange L, Deng Z, Zhao Q, Perosanz F, Romero I, Noll C, Schmid R, Rothacher M, Thaller D, Steigenberger P (2005) Absolute phase center corrections of satellite and receiver antennas: impact on global GPS solutions and estimation of azimuthal phase center variations of the satellite antenna. GPS Solut 9:283–293
Montenbruck O, Hauschild A, Steigenberger P, Langley RB (2010) Three's the challenge: a close look at GPS SVN62 triple frequency signal combinations finds carrier-phase variations on the new L5. GPS World 21(8):819
Pan L, Zhang X, Li X, Liu J, Li X (2017) Characteristics of inter-frequency clock bias for Block IIF satellites and its effect on triple-frequency GPS precise point positioning. GPS Solut 21(2):811–822
Pan L, Zhang X, Guo F, Liu J (2019) GPS inter-frequency clock bias estimation for both uncombined and ionospheric-free combined triple-frequency precise point positioning. J Geod 93:473–487
Saastamoinen J (1973) Contributions to the theory of atmospheric refraction. Bull Géod 107(1):13–34. https://doi.org/10.1007/BF02522083
Stürze A, Weber G (2017) The multi-GNSS experiment (MGEX) of the international GNSS service (IGS) – achievements. Prosp Chall, Adv Space Res 59(7):1671–1697
Urlichich Y, Subbotin V, Stupak G, Dvorkin V, Povalyaev A, Karutin S (2011) GLONASS Modernization.in: Proceedings of the 24th international technical meeting of the satellite division of the institute of navigation (ION GNSS 2011), Portland, OR, 2011, pp. 3125–3128
Zaminpardaz S, Teunissen PJG, Nadarajah N (2017) GLONASS CDMA L3 ambiguity resolution and positioning. GPS Solut 21(2):535–549
Zaminpardaz S, Teunissen PJG, Khodabandeh A (2021) GLONASS–only FDMA+CDMA RTK: performance and outlook. GPS Solut 25(3):1–12
Zeng T, Sui L, Ruan R, Jia X, Tian Y, Zhang B (2021) Estimation of GPS satellite antenna phase center offsets of the third frequency using raw observation model. Adv Space Res 68(8):3268–3278
Zhang F, Chai H, Li L, Wang M, Feng X, Du Z (2022) Understanding the characteristic of GLONASS inter-frequency clock bias using both FDMA and CDMA signals. GPS Solut 26(2):1–7
Zhang F, Chai H, Wang M, Bai T, Li L, Guo W, Du Z (2023) Considering inter-frequency clock bias for GLONASS FDMA + CDMA precise point positioning. GPS Solut 27(1):10

Publisher's Note Springer Nature remains neutral with regard to jurisdictional claims in published maps and institutional affiliations.

Jiaqi Wu is currently a Ph.D. candidate at the School of Geodesy and Geomatics at Wuhan University, specializing in geodesy and surveying engineering. He completed his M.S. degree at the School of Geodesy and Geomatics at Wuhan University in 2020. His area of research currently focuses on GNSS precise orbit determination and precise point positioning.

Xingxing Li is currently a professor at Wuhan University. He has completed his B.Sc. degree at the School of Geodesy and Geomatics of Wuhan University and a Ph.D. at the Department of Geodesy and Remote Sensing of the German Research Centre for Geosciences (GFZ). His current research mainly involves GNSS precise data processing and its application for geosciences.

Yongqiang Yuan is a post-doctor at the School of Geodesy and Geomatics at Wuhan University. He obtained his Ph.D. at the School of Geodesy and Geomatics at Wuhan University in 2022. His area of research currently focuses on GNSS precise orbit determination (POD) and geodetic parameter estimation with GNSS observations.

Xin Li is a post-doctor at the School of Geodesy and Geomatics at Wuhan University. She obtained her Ph.D. at the School of Geodesy and Geomatics at Wuhan University in 2021. Her area of research currently focuses on multi-GNSS precise point positioning, multi-frequency ambiguity resolution, and multi-sensor fusion navigation technology.

Hongjie Zheng is currently a Ph.D. candidate at the School of Geodesy and Geomatics at Wuhan University, specializing in geodesy and surveying engineering. He has completed his B.Sc. at the School of Geodesy and Geomatics at Wuhan University in 2019. His area of research currently focuses on GNSS bias estimation and real-time precise orbit determination.

Wei Zhang is currently a Ph.D. candidate at the School of Geodesy and Geomatics at Wuhan University, specializing in geodesy and surveying engineering. He has completed his M.S. at the School of Geodesy and Geomatics at Wuhan University in 2021. His area of research currently focuses on GNSS bias estimation and precise orbit determination.